ACS APPLIED ENERGY MATERIALS

www.acsaem.org Article

Origin of Electronic Modification of Platinum in a Pt_3V Alloy and Its Consequences for Propane Dehydrogenation Catalysis

Stephen C. Purdy, Pushkar Ghanekar, Garrett Mitchell, A. Jeremy Kropf, Dmitry Y. Zemlyanov, Yang Ren, Fabio Ribeiro, W. Nicholas Delgass, Jeffrey Greeley, and Jeffrey T. Miller*

Cite This: *ACS Appl. Energy Mater.* 2020, 3, 1410−1422 Read Online

ACCESS | Metrics & More | Article Recommendations | Supporting Information

ABSTRACT: We demonstrate the synthesis of a Pt_3V alloy and Pt/Pt_3V core/shell catalysts, which are highly selective for propane dehydrogenation. The selectivity is a result of the Pt_3V intermetallic phase, which was characterized by in situ synchrotron XRD and XAS. Formation of a continuous alloy surface layer 2−3 atomic layers thick was sufficient to obtain identical catalytic properties between a core−shell and full alloy catalyst, which demonstrates the length scale over which electronic effects pertinent to dehydrogenation act. Electronic characterization of the alloy phase was investigated by using DFT, XPS, XANES, and RIXS, all of which show a change in the energy of the filled and unfilled Pt 5d states resulting from Pt−V bonding. The electronic modification leads to a change in the most stable binding site of hydrocarbon fragments, which bind to V containing ensembles despite the presence of 3-fold Pt ensembles in Pt_3V. In addition, electronic modification destabilizes deeply dehydrogenated species thought to be responsible for hydrogenolysis and coke formation.

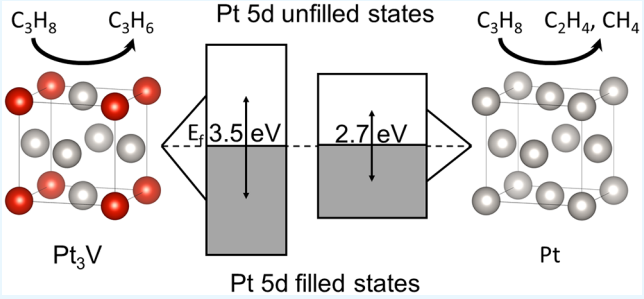

KEYWORDS: *propane dehydrogenation, dehydrogenation selectivity, Pt_3V nanoparticle, intermetallic alloy catalyst, resonant inelastic X-ray scattering, in situ synchrotron X-ray diffraction, in situ X-ray absorption spectroscopy, electronic effects in alloy catalysts*

INTRODUCTION

Alloy catalysts have been extensively studied for many catalytic reactions due to their improved performance over their monometallic constituents.[1] In particular, alloy catalysts have seen extensive use for dehydrogenation of light alkanes for the production of olefins. Monometallic catalysts such as Pt suffer from low olefin selectivity due high hydrogenolysis activity.[2] Industrially, an alloy of Pt and Sn is often used for propane and butane dehydrogenation and offers improved selectivity and stability over a Pt only catalyst.[3] Interest in alloy catalysts for on-purpose light alkane dehydrogenation has also been fueled by decreased supply of propylene due to naphtha crackers switching to an ethane feedstock and the widespread production of shale gas which contains a significant fraction of C_2+ alkanes.[4] New alloy catalysts with higher selectivity will allow for more efficient utilization of the C_2+ fraction of shale gas which will increasingly be used in on-purpose dehydrogenation plants. A major goal in the research of alloy catalysts for dehydrogenation is to understand the electronic and geometric factors responsible for the increased selectivity to olefins.

The formation of an alloy between Pt and a second promoter metal leads to changes in the electronic and structural properties of the catalyst. The electronic effect is usually explained by extending Hammer and Nørskov's d-band theory to alloys, in which the promoter element shifts the d-band center away from the Fermi energy, leading to a decrease in binding strength of adsorbates.[5,6] Experimentally, it has been observed that alloy formation with Pt causes a decrease in the heat of adsorption of alkenes, resulting in the product desorption pathway becoming more favorable than deep dehydrogenation and coking.[7,8] Density functional theory (DFT) studies on Pt and Pt−Sn surfaces have come to similar conclusions.[9,10]

While the qualitative effect of shifting electronic states with respect to the Fermi energy is generally agreed upon, other aspects of how the promoter modifies the electronic properties of alloys, such as the effect of charge transfer, are still debated. Spectroscopic changes between pure metals and alloys are often explained by electron transfer to or from the d-band driven by electronegativity difference.[11−13] An observed increase in the Pt L_3 edge X-ray absorption near edge structure (XANES) edge energy and decrease in the Pt 4d binding energy measured by X-ray photoelectron spectroscopy (XPS) seen in alloys has been interpreted as a donation of electron

Received: September 20, 2019
Accepted: January 7, 2020
Published: January 7, 2020

density from the promoter to Pt. The donation of electron density further fills the d-band, and the shift of the d-band center and the resulting decrease in the binding strength of alkenes are cited as being responsible for the improved selectivity.[11,12] While charge partitioning on alloys generally shows a subunity change in the total number of electrons between atoms in a pure metal and an alloy, alloys generally show a negligible change in the d-band filling, which would preclude electron transfer from significantly modifying adsorbate bonding.[5,14,15] Alternative explanations for the spectroscopic shifts not involving electron transfer have been suggested involving broadening of the d-band.[16,17] However, arguments both for and against charge transfer generally rely on theoretical calculations and a single spectroscopic technique that indirectly probes the filled valence d-states responsible for catalysis.

Recently, Cybulskis et al. used resonant inelastic X-ray scattering (RIXS) spectroscopy to experimentally measure the energy change of the 5d electrons between Pt and Pt in a Pt_1Zn_1 (AuCu structure) alloy.[18] They found that alloy formation with Zn leads to an upward shift in the energy of the unfilled states and a downward shift in the energy of the filled state. DFT results showed that the d-band center in Pt_1Zn_1 is minimally shifted (~0.1 eV) relative to Pt. The change in the energy of the filled and unfilled Pt 5d states was cited as responsible for observed changes in the turnover rate (TOR), while isolation of active sites by zinc was responsible for the increased selectivity.

Regardless of whether electron transfer or changing electron energy underlie the electronic effect, a Pt alloy with a large d-band shift should have a large electronic effect and should lead to improved performance over monometallic Pt. Additionally, an alloy with a large d-band shift should also show easily discernible spectroscopic shifts relative to the pure metal, allowing for unambiguous trends among multiple spectroscopic techniques. Pt and V have a larger electronegativity difference than do other widely studied alloys such as Pt−Sn. Finally, computational and experimental studies on Pt−V alloys show large shifts in the d-band center, and thus should display large changes in the electronic properties of Pt.[5,19] Pt−V alloys, however, have not been previously studied as dehydrogenation catalysts, possibly because Pt−V alloys are difficult to synthesize, requiring oxygen free synthesis and strong reducing agents.[20]

Herein, we demonstrate that Pt_3V nanoparticles significantly improve selectivity to propylene as compared to unalloyed Pt. The structural ordering of the nanoparticles is confirmed by in situ X-ray absorption spectroscopy (XAS) and in situ synchrotron X-ray diffraction (XRD). The corresponding changes in the electronic properties are determined by using DFT, RIXS, XPS, and XANES. DFT calculations demonstrate that the binding strengths of prototypical intermediates involved in coking and dehydrogenation decrease appreciably due to presence of V promoter. Additionally, the electronic structure of Pt atoms also changes with increasing V incorporation as evidenced from projected density of states (pDOS) analysis of Pt d-states. In agreement with DFT, the XPS, XANES, and RIXS show that the electronic modification results from a decrease in the energy of the filled Pt 5d orbitals, rather than due to a change in the number of d-electrons.

EXPERIMENTAL SECTION

Catalyst Synthesis. Pt−V catalysts were supported on Davisil grade 646 silica (35−60 mesh, Sigma-Aldrich) and synthesized by sequential incipient wetness impregnation. Pt and V loadings are given in weight percent with respect to the total catalyst mass. V impregnation to give a 5% V on silica catalyst was done by using a solution of 1:2 molar ratio of ammonium metavanadate to oxalic acid. 0.574 g of ammonium metavanadate and 0.884 g of oxalic acid dihydrate were dissolved in 4 mL of Millipore water. The oxalic acid/ammonium metavanadate solution was heated to 100 °C, refluxed for 1 h, and then added dropwise to 5 g of silica. The impregnated silica was dried overnight at 125 °C and then calcined at 350 °C for 3 h in flowing air.

Pt was added to the V−SiO_2 by incipient wetness impregnation of a pH adjusted solution of tetraamine platinum(II) nitrate. The solution pH was adjusted to 11 with ammonium hydroxide. After impregnation of the Pt salt, the catalyst was dried overnight at 125 °C and calcined at 250 °C for 3 h in flowing air. The mass of tetraammine platinum nitrate used in the impregnation solution was adjusted to give Pt loadings of 2% and 5% on the bimetallic catalysts and a separate monometallic Pt catalyst with a Pt loading of 3%. After calcination, catalysts were reduced in 5% H_2 with a slow heating ramp (2.5 °C/min) through 250 °C and a fast ramp to 550 °C with a 30 min dwell at temperature. The reduced catalysts were then cooled to room temperature in nitrogen and passivated in air. Other Pt−V catalysts were synthesized with different metal loadings of each component with full details given in Table S1 of the Supporting Information.

Electron Microscopy. Particle size distributions were measured by scanning transmission electron microscopy (STEM) and are reported as volume average particle sizes. Imaging was performed on a FEI Titan at an accelerating voltage of 300 keV in STEM mode by using a high angle annular dark field detector. Particle size distributions were measured by counting over 250 particles per sample. Energy-dispersive X-ray spectroscopy (EDS) maps were taken on a FEI Talos F200X S/TEM with an X-FEG high brightness electron source and a Super-X EDS system. The microscope was operated at an accelerating voltage of 200 keV and has a maximum STEM resolution of 1.2 Å and a maximum EDS mapping resolution of 1.6 Å.

Propane Dehydrogenation. Catalytic measurements were performed on a laboratory scale fixed bed microreactor. 0.025−0.25 g of catalyst was diluted to 1 g total mass with Davisil grade 646 (35−60 mesh) and loaded into a quartz tube for testing, creating a catalyst bed approximately 2−3 cm in length. A stainless-steel thermocouple well was inserted into the bottom of the catalyst bed to monitor temperature during reactions. Four mass flow controllers (Parker) were used to supply reactant gases to the reactor. Effluent gas was analyzed by an online HP 6890 gas chromatograph equipped with an FID detector and a Restek Alumina BOND/Na_2SO_4 capillary column. Full separation of C_1 through C_3 products was accomplished in 5 min.

The selectivity to propylene and propane conversion were calculated on a carbon basis of gas phase products. Dehydrogenation turnover rates were normalized based on the fraction of surface Pt determined by surface oxidation difference extended X-ray absorption fine structure (EXAFS) (described below). Catalysts were pretreated at 550 °C in 5% H_2, and the reactor was purged with N_2 before flowing reactant gases. A first-order exponential decay function was fit to time on stream data to determine selectivity and conversion for each test at zero deactivation. Each conversion, selectivity, and initial turnover rate reported was determined by using a fresh sample from the same respective batch of each prereduced catalyst.

X-ray Absorption Spectroscopy (XAS). Pt L_3 edge in situ XAS was performed at the MRCAT bending magnet line (10BM) at Argonne National Laboratory's Advanced Photon Source. Measurements were taken in transmission mode using a set of three ion chambers for simultaneous measurement of a sample and an energy reference foil. Powder samples pressed into a stainless steel sample holder were treated and measured in a quartz tube reactor with X-ray

https://dx.doi.org/10.1021/acsaem.9b01373
ACS Appl. Energy Mater. 2020, 3, 1410−1422

transparent windows. Before measurement, samples were reduced at 550 °C in 3.5% H_2 for 30 min. The reactor was then purged with ultrahigh-purity helium passed through an oxygen trap at temperature to desorb hydrogen and cooled to room temperature for measurement. Scans were also collected after exposing the reduced samples to air at room temperature.

To study the surface layer of the Pt−V nanoparticles, EXAFS difference spectra were used. EXAFS spectra of the catalyst oxidized in air at room temperature and that of the catalyst in the reduced state were subtracted to give the difference. Air exposure at room temperature oxidizes the surface layer of Pt nanoparticles.[21] The unchanged spectral features of the particle core common to both the reduced and surface oxidized samples are removed in the difference, leaving only the changes resulting due to the surface oxidation process. Details of the data processing for EXAFS difference spectra and EXAFS fitting are given in the Supporting Information.

Resonant Inelastic X-ray Scattering (RIXS). RIXS measurements were performed at the MRCAT insertion device line (10ID). RIXS measurements were performed on catalyst wafers treated in an in situ fluorescence cell described elsewhere.[22] Measurements were conducted at 100 °C after a 30 min pretreatment at 550 °C in 3.5% H_2. The RIXS process measured was the Lβ_5 fluorescent emission (Pt 5d decay to $2p_{3/2}$ core hole) resonant about the Pt L_3 absorption edge (Pt $2p_{3/2}$ to 5d unfilled). X-ray absorption at the Pt L_3 edge was measured in transmission by using a set of ion chambers. Simultaneously, high-resolution X-ray emission spectra of the Pt Lβ_5 fluorescence line were collected by using a wavelength dispersive spectrometer based on a bent silicon crystal. Full details of the emission spectrometer and data processing are given in the Supporting Information.

X-ray Photoelectron Spectroscopy (XPS). XPS analysis was performed by a Kratos Axis Ultra Imaging DLD spectrometer with an attached pretreatment chamber. The XPS spectra were collected by using a monochromatic Al Kα (1486.69 eV) radiation and a hemispherical electron energy analyzer operated with a constant pass energy of 20 eV. Charge neutralization was used to mitigate nonhomogeneous charging and to improve resolution. Prior to measurement, samples were pretreated at 550 °C in 5% hydrogen for 30 min. The pretreatment chamber was then evacuated, and the sample was transferred under ultrahigh vacuum to the analysis chamber. XPS spectra were processed by using CasaXPS software. The Pt 4f peaks were fit by using an asymmetric Lorentzian function (LF(a,b,c,d) function in CasaXPS) after subtraction of a Shirley background. Charge correction was performed by setting the Si 2p binding energy to 103.7 eV.

X-ray Diffraction (XRD). In-situ synchrotron XRD spectra were collected at the 11-ID-C beamline at the Advanced Photon Source. XRD experiments were performed in transmission geometry, using an X-ray energy of 106.257 keV (0.11684 Å) and a PerkinElmer large area detector. Pressed catalyst wafer samples were loaded into a water-cooled Linkam stage, which allowed for heating and cooling as well as gas flow. Samples were pretreated identically to XAS measurements. Scans of the empty Linkam cell and bare silica support were collected for background subtraction. The collected 2D diffraction patterns were calibrated by using a CeO_2 standard sample and integrated to give standard powder diffraction data by using Fit2D software.[23,24] Theoretical XRD patterns were calculated by using crystallographic references and the Materials Analysis Using Diffraction (MAUD) software.[25] Multiple peak fitting was performed with OriginPro software using a mixed Gaussian−Lorentzian peak profile.

Density Functional Theory (DFT). Electronic structure calculations were performed using periodic, self-consistent DFT, as implemented within the Vienna ab Initio Simulation Package (VASP).[26−29] Projector augmented wave pseudopotentials[30] and the PBE functional for exchange and correlation[31] were used, which have been extensively benchmarked for transition metals and have been shown to provide good predictions of trends in adsorption properties across different metal surfaces. Lattice constant optimization and bulk binary phase diagram calculations were performed using a plane wave cutoff energy of 600 eV and a 10 × 10 × 10 Monkhorst−Pack **k**-point grid and Methfessel−Paxton smearing.[32,33] Lattice constants were converged with a force criterion of 0.02 eV/Å, giving a lattice constant of 3.98 Å for Pt and 3.92 Å for Pt_3V.

Surface calculations for adsorption energies were conducted on close-packed (111) facets with supercells of Pt and Pt_3V having side lengths of $\sqrt{12}$ times those of the primitive unit cell. A plane wave cutoff of 500 eV and a 4 × 4 × 1 Monkhorst−Pack **k**-point grid with Methfessel−Paxton smearing were used. The slabs were composed of five layers with the bottom two layers constrained to represent the bulk. For comparison, binding energies of CO and CH_3 species were also calculated on a smaller 2 × 2 × 5 unit cell with the same number of layers relaxed, and no differences were found (see the Supporting Information for additional details). We note that although such single crystal models may not capture all quantitative aspects of the structure and reactivity of transition metal alloy nanoparticles, they provide reasonable descriptions of qualitative trends, which is the goal of this study. All calculations were spin polarized, and a dipole correction was employed perpendicular to slab surface to reduce periodic image interactions.

Projected density of states (pDOS) calculations were conducted on (111) close-packed surfaces with 2 × 2 × 5 supercells and three layers relaxed. Pure Pt(111), bulk-terminated Pt_3V (111), and Pt(111) with one and two monolayers of Pt_3V skins on the surface were considered for the pDOS analysis. For these calculations, a plane wave cutoff of 800 eV, a denser **k**-point grid of 13 × 13 × 1, and tetrahedron Blöchl smearing were used. The density of states was projected according to the Wigner−Seitz radius provided by the PAW potential. The DOS was evaluated on 800 grid points in a range of ±8 eV from the corresponding Fermi energy for the system. Methfessel−Paxton smearing with a width of 0.2 eV was used to generate a smoother pDOS. The Pt d-band center was calculated as the first moment of the pDOS of d-electrons for surface Pt atoms, and the d-band width was evaluated as the square root of its second moment.

Transition-state (TS) energy calculations were performed with CI-NEB where each optimized TS structure was checked with a normal-mode analysis to ensure that only a single imaginary frequency exists.[34] Gas phase species were calculated with a plane wave cutoff of 500 eV with Gaussian smearing and a gamma **k**-point within a 20 × 21 × 22 Å supercell. For setup, visualization, and analysis of atomistic simulations, Atomic Simulation Environment (ASE) was used.[35] Rendering of the atomic configuration was done using OVITO.[36]

RESULTS

Structural Characterization. Metal nanoparticle sizes of the 3Pt, 5Pt−5V, and 2Pt−5V catalysts were determined by STEM imaging (Figure S1). The volume average particle sizes for 3Pt, 5Pt−5V, and 2Pt−5V were 2.6 ± 0.5, 2.2 ± 0.5, and 2.2 ± 0.7 nm, respectively. STEM EDS maps of 2Pt−5V (Figure S2) of Pt and V show a highly dispersed V on the support and particles containing both Pt and V. The TEM images do show some amount of particle size heterogeneity, likely due to sintering and coalescence resulting from the high-temperature reduction done as part of the synthesis process.

XAS was used to verify that V incorporates into the metallic Pt particles and forms a bimetallic phase. From the V K edge (Figure S3), only scattering from nearest-neighbor V−O and second shell V−O−V is evident after reduction of the 5Pt−5V catalyst, suggesting most of the V is present as oxide clusters. Figure 1 shows the R-space magnitude and imaginary components of the Pt L_3 EXAFS for 3Pt (black) and 2Pt−5V (blue). 3Pt shows the three peaks characteristic of scattering from metallic Pt. Compared to 3Pt, the first peak in the 2Pt−5V sample at 2 Å (phase uncorrected distance) increases slightly in intensity, and the third peak at 3 Å (phase uncorrected distance) decreases slightly in intensity. Additionally, the peaks in 2Pt−5V shift to lower *R* compared to 3Pt. The changes in the first shell scattering peaks are due to Pt−V

https://dx.doi.org/10.1021/acsaem.9b01373
ACS Appl. Energy Mater. 2020, 3, 1410−1422

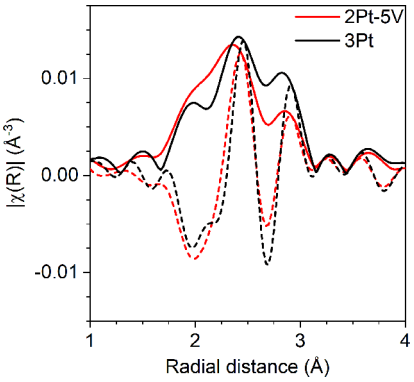

Figure 1. In-situ Pt L_3 edge EXAFS magnitude (solid lines) and imaginary (dashed lines) of 3Pt (black) and 2Pt−5V (red) catalysts. Spectra were collected at room temperature in He after a 30 min reduction at 550 °C in 3.5% H_2.

scattering, confirming that a Pt−V bimetallic forms. Fits of the first shell EXAFS and XANES edge energies are shown in Table 1.

Table 1. XANES Edge Energies and EXAFS Fitting Parameters for 3Pt, 5Pt−5V, and 2Pt−5V: Coordination Number (CN), Bond Distance (R), Debye−Waller Factor (σ^2), and E_0 Correction

sample	XANES edge energy (eV)	scattering pair	CN	R (Å)	σ_2 (Å^2)	E_0 (eV)
3Pt	11564.0	Pt−Pt	8.8	2.74	0.002	−0.9
5Pt−5V	11564.2	Pt−Pt	6.5	2.73	0.003	−0.8
		Pt−V	2.0	2.71	0.003	2.6
2Pt−5V	11564.4	Pt−Pt	6.2	2.72	0.003	−1.6
		Pt−V	2.9	2.72	0.003	2.3

For 3Pt, a high-quality fit was obtained by fitting with a single Pt−Pt scattering path. To fit the Pt−V catalysts, it was necessary to include a second scattering path (Pt−V) to fit the data. The total coordination number, which is correlated to the metal particle size,[37] of all three catalysts is close to 9, which agrees with the STEM results showing that all three catalysts have similar particle sizes (2−2.5 nm). The bond distance of 2.74 Å in the 3Pt sample is characteristic of small Pt nanoparticles, where the decrease in average coordination number causes a slight contraction of the Pt−Pt bond distance from the bulk value of 2.77 Å.[38] In the Pt−V catalysts, the Pt−Pt bond distance was also contracted, with 5Pt−5V having a bond distance of 2.73 Å and 2Pt−5V having a Pt−Pt bond distance of 2.72 Å. For both alloy samples, the Pt−V bond distance for each sample was the same as the respective Pt−Pt bond distance. Fit parameters and spectra for other Pt−V catalysts discussed in the Experimental Methods synthesis section are given in Table S2 and Figure S4, respectively and have bond distances and coordination numbers similar to the above-described Pt−V catalysts.

The ratio of Pt−V to Pt−Pt neighbors is related to the particle composition. By nature of their fixed composition, Pt−V intermetallic phases have fixed values of the neighbor ratio, and hence the ratio can be used to determine whether a sample has a local Pt environment consistent with a given alloy phase. Of the possible Pt−V alloys only Pt_8V and Pt_3V have Pt−Pt bonds. Pt_8V has a Pt−V/Pt−Pt neighbor ratio of 0.2, and Pt_3V has a Pt−V/Pt−Pt neighbor ratio of 0.5. The 5Pt−5V catalyst had a Pt−Pt coordination number of 6.5 and a Pt−V coordination number of 2, leading to a ratio of Pt−V to Pt−Pt neighbors of 0.31, which is Pt rich with respect to Pt_3V. An intermediate neighbor ratio could be explained by a mixture of two phases as would be present in core−shell particles. The 2Pt−5V catalyst had a Pt−Pt coordination number of 6.2 and a Pt−V coordination number of 2.9, giving a Pt−Pt/Pt−V coordination number ratio of 0.47, which closely matches the ratio of Pt_3V.

In a 5Pt−5V catalyst reduced at 200 °C from the freshly calcined state the coordination number ratio closely matches that of 5Pt−5V reduced at 550 °C (Figure S5 and Table S2), albeit with a lower total coordination number. Based on the color change of the catalyst during reduction from brown to black, the onset of platinum reduction on silica supported Pt−V catalysts is close to 200 °C. The presence of Pt−V scattering in 5Pt−5V early in the reduction process suggests that vanadium reduction and incorporation occur early or simultaneously with the nucleation of metallic Pt. The similarity in composition between the 5Pt−5V catalyst reduced at 200 and 550 °C suggests that the particle size heterogeneity in the high-temperature reduction sample does not also accompany a compositional heterogeneity.

To study the long-range order and phase composition of the Pt−V nanoparticles, in situ synchrotron XRD was used. Synchrotron XRD provides several advantages over laboratory-based XRD, including improved signal-to-noise and the ability to use a high X-ray energy which further suppresses the contribution of the amorphous support for the spectrum. As a result of the high X-ray energy used (106.257 keV), diffraction peaks occur at a lower angle and a lower angular range than typical of a laboratory instrument.

Distinguishing between Pt and Pt_3V is difficult due to the small difference in their unit cell parameters: 3.92 Å for Pt and 3.87 Å for Pt_3V.[39] Additionally, below 10 nm, the lattice parameters of both Pt and Pt_3V change with particle size due to the contraction of bond distance that occurs in nanoparticles. Leontyev et al. used synchrotron XRD to measure the lattice parameter contraction in Pt nanoparticles of different size.[40] At 2 nm in size, the lattice parameter of Pt nanoparticles decreased from the bulk value by 0.03 Å, a decrease comparable in size to the lattice parameter difference between Pt and Pt_3V (0.05 Å). Because both V incorporation and decreasing particle size each decrease the lattice parameter, changes cannot be solely attributed to composition unless a comparison is made between a Pt and Pt−V particle of similar size.

Figure 2a shows the in situ synchrotron XRD pattern of 3Pt and 5Pt−5V. The fundamental lines characteristic of an fcc metal are present, ruling out the presence of Pt−V phases without fcc symmetry, such as Pt_8V, PtV, or Pt_2V. The XRD peaks are broad and weak in intensity due to the small average particle size present in the sample, as described above. In the high Pt loading sample (5Pt−5V), no diffraction from a crystalline vanadium oxide phase is observed; while weak vanadium oxide diffraction peaks are seen in the sample with lower Pt loading. Both samples, however, have similar shifts in the position of fcc reflections (2Pt−5V, Figure S6). Figure 2b shows details of the 220 and 311 reflections for 3Pt and 5Pt−5V after a reduction treatment at 550 °C. While the peak shifts between 3Pt and 5Pt−5V are small (0.03° for the 220 peak), the shift is larger than the angular resolution of the instrument (0.005°) and is more apparent in the high index diffraction

https://dx.doi.org/10.1021/acsaem.9b01373
ACS Appl. Energy Mater. 2020, 3, 1410−1422

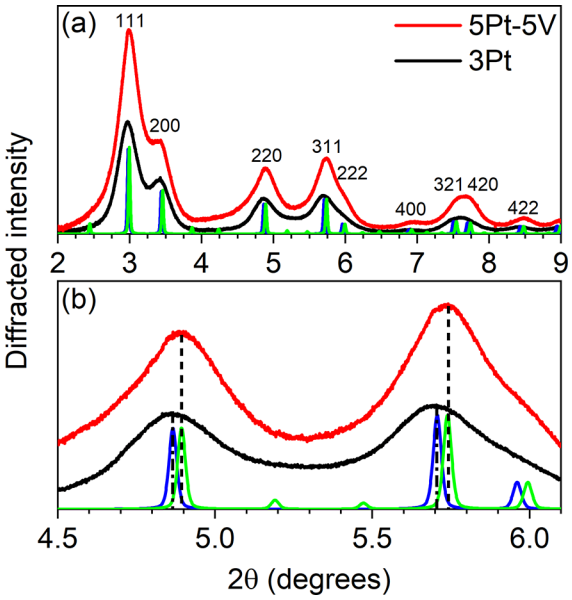

Figure 2. (a) In-situ synchrotron XRD patterns of 3Pt (black), 5Pt−5V (red). Fundamental fcc lines are labeled in black. Simulated patterns of Pt with a lattice parameter of 3.89 Å (blue) and Pt_3V with a lattice parameter of 3.87 Å (green). (b) Expanded view of the 220 and 311 reflection for the above samples with vertical dashed lines denoting experimental peak positions. All experimental spectra were collected at 35 °C in 3.5% H_2 after reduction at 550 °C.

peaks. Particle size dependent lattice contraction is controlled for by measuring a monometallic and alloy catalyst of the same particle size, and the shift in peak position is attributed to formation of the Pt_3V phase. The peak positions of the 3Pt catalyst agree with the simulated Pt pattern with a lattice parameter of 3.89 Å. The peak positions of the 5Pt−5V catalyst are shifted to higher angle than the 3Pt catalyst. Simulating a Pt_3V pattern with a lattice parameter of 3.87 Å gives excellent agreement with the peak positions of the 5Pt−5V sample across the entire pattern. The lattice parameter for 5Pt−5V is larger than expected for a nanoparticle Pt_3V catalyst which would be contracted from the bulk lattice parameter of 3.87 Å. The difference is explained by the EXAFS results for 5Pt−5V showing that it is Pt-rich with respect to Pt_3V, which would give a lattice parameter intermediate between Pt and Pt_3V. In other Pt−V catalysts that are more Pt-rich (Figure S7), XRD shows asymmetric peak shapes, indicating two phases are present. When fit with two components (Table S3), the peak and shoulder give lattice parameters matching that of Pt (3.89−3.90 Å) and Pt_3V (3.87−3.88 Å), respectively.

Electronic Characterization. As the 5Pt−5V sample was determined to be a phase mixture, further electronic characterization was carried out on the 2Pt−5V, which had a coordination number ratio closely matching Pt_3V, which suggests that 2Pt−5V is a pure phase Pt_3V alloy. Figure 3a shows the Pt L_3 edge XANES for 3Pt and 2Pt−5V after reduction in 3.5% H_2 at 550 °C. The edge energy (measured as the energy of the first zero crossing of the second derivative of the XANES) for the 3Pt catalyst was identical to the concurrently measured foil value of 11.5640 keV. The edge energy of 2Pt−5V was shifted 0.4 eV higher than the Pt foil. The white line shape of 2Pt−5V is also different than the 3Pt catalyst which has a similar particle size, becoming narrower and higher in intensity. The changes reflect the difference in the energy distribution of the unfilled states between the monometallic and alloy catalysts.

Figure 3b shows the Pt 4f high-resolution XPS spectra of 3Pt and 2Pt−5V. Fitting parameters for the Pt 4f high resolution XPS spectra are given in Table S4. The binding energies for 3Pt and 2Pt−5V from fitting were 70.9 and 71.3 eV, respectively. Pt metal has a Pt $4f_{7/2}$ binding energy of 71.0 eV with an asymmetric peak shape toward higher binding energy, while platinum oxides have higher binding energies between 73 and 75 eV with a symmetric peak shape.[41] The asymmetric peak shape and binding energy for both samples are consistent with Pt in the metallic state. The core level shift (CLS) for 2Pt−5V is calculated as the difference in binding energy between the pure metal (3Pt) and the alloy, giving an increase in binding energy of 0.4 eV.

RIXS is a two-photon spectroscopy where an electron is photoexcited from a core state to a vacant valence state (here a Pt 5d unfilled state) and an emitted photon is measured arising from an electron in the filled valence state (Pt 5d filled state) filling the core hole. To probe the energy of the Pt 5d electrons, the Lβ_5 emission line, which corresponds to the decay of a 5d electron into a $2p_{3/2}$ core hole, is selectively measured. When the incident photon is scattered elastically (i.e., the photoexcited $2p_{3/2}$ electron decays back into the $2p_{3/2}$

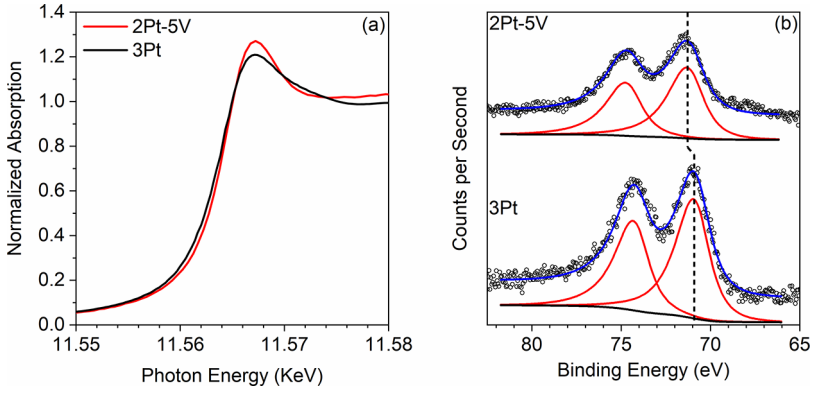

Figure 3. (a) In-situ Pt L_3 edge XANES of 3Pt (black) and 2Pt−5V (red). Spectra were collected at room temperature in He after reduction at 550 °C in 3.5% H_2 for 30 min and a subsequent purge in He at 550 °C. (b) High-resolution Pt 4f XPS spectra of 2Pt−5V and 3Pt after a reduction treatment in 5% H_2 at 550 °C for 30 min. Black circles: raw data; black line: Shirley background; red lines: component fits; blue line: total fit. Background and components are offset for clarity. The vertical line denotes the peak position of the Pt $4f_{7/2}$ component of 3Pt and 2Pt−5V.

https://dx.doi.org/10.1021/acsaem.9b01373
ACS Appl. Energy Mater. 2020, 3, 1410−1422

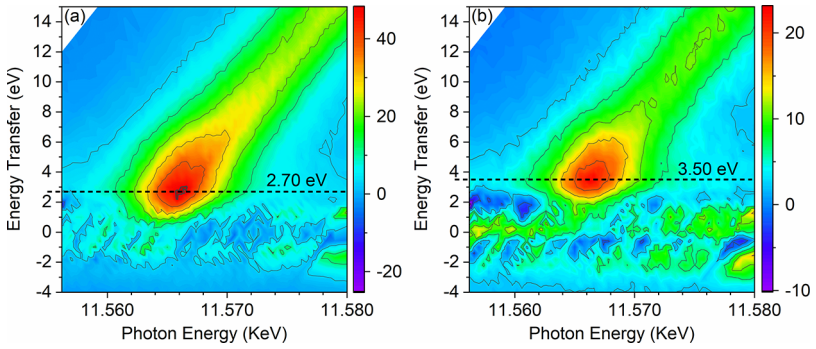

Figure 4. Pt L_3−$L\beta_5$ RIXS maps of Pt (a) and Pt_3V (b). Spectra were collected after a reduction treatment at 550 °C in 3.5% H_2 for 30 min. Spectra were collected at 100 °C in 3.5% H_2. Horizontal dashed lines denote the maximum of the inelastic scattering peak for each sample.

core hole), the fluoresced photon energy is equal to the incident photon energy, which gives a peak at an energy transfer value of 0 eV. For clarity, the elastic scattering line has been subtracted from the RIXS plots in Figure 4. Intensity fluctuations around an energy transfer value of 0 eV are artifacts from the subtraction of the elastic scattering line. Inelastic scattering occurs when the fluorescent decay into the $2p_{3/2}$ core hole occurs by an electron other than the excited $2p_{3/2}$ electron. This can occur by any symmetry allowed electron transition according to dipole selection rules.

RIXS spectra are plotted as the fluoresced intensity as a function of the incident photon energy on the abscissa and the energy difference between the incident and emitted photon (energy transfer) on the ordinate. The inelastic scattering peak manifests as a broad maximum centered at an incident energy value between the respective XANES edge energy and white line energy for each sample. Far from the XANES inflection point (~5 eV), the resonant enhancement of the $L\beta_5$ emission mode decays, leading to a low-intensity tail toward higher energy transfer values with increasing incident energy. For the Pt sample, the maximum of the inelastic scattering peak lies at an incident energy of 11.5640 keV and an energy transfer value of 2.7 eV. This corresponds to an energy separation of 2.7 eV between the average energy of the filled and unfilled states. For Pt_3V, the maximum of the inelastic scattering peak lies at an incident energy of 11.5644 keV, with an energy transfer value of 3.5 eV. The energy separation between the filled and unfilled states in Pt_3V is 0.8 eV larger than Pt. From the XANES edge energy of pure phase Pt_3V (2Pt−5V) the 0.8 eV split can be separated into a 0.4 eV increase in the energy of the unfilled states and a 0.4 eV decrease in the energy of the filled 5d states relative to Pt.

Propane Dehydrogenation. Figure 5 shows propylene selectivity and propane conversion extrapolated to zero deactivation for 3Pt, 5Pt−5V, and, 2Pt−5V with each data point representing a separate sample of catalyst from the same synthetic batch. For all reactions, propylene was the main product; hydrogenolysis led to the formation of methane, ethane, and ethylene. Tests performed without cofed hydrogen are shown in Figure 5a. The selectivity of 2Pt−5V and 5Pt−5V were equivalent in tests without hydrogen, both showing above 95% propylene selectivity which did not decrease with increasing conversion. In comparison, 3Pt showed moderate selectivity which decreased as the conversion increased.

Figure 5b shows catalyst tests performed with cofed hydrogen. Dehydrogenation in the presence of H_2 is a more demanding test of the catalysts' selectivity as the latter is required for hydrogenolysis. The propane-to-hydrogen ratio

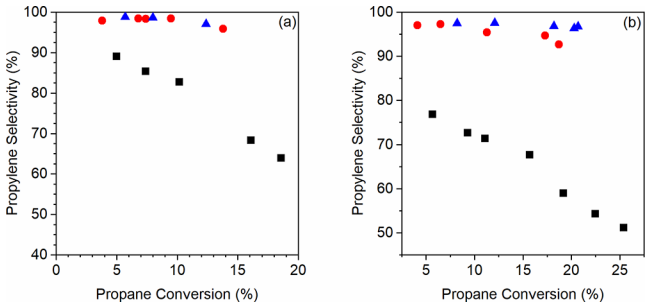

Figure 5. Propylene selectivity and propane conversion for 3Pt (black squares), 5Pt−5V (red circles), and 2Pt−5V (blue triangles) tested without (a) and with (b) cofed H_2. Reactions were performed at 550 °C at 3 psig with 2.5% propane balance N_2. For (b) the hydrogen concentration was 2.5%. Data points shown are at zero deactivation with each data point representing a separate test.

was 1:1. Similar to the tests done without hydrogen, 3Pt decreased in selectivity with increasing conversion, but the selectivity at low conversion when tested with hydrogen was lower than when tested without. For the 2Pt−5V catalyst, cofeeding hydrogen did not change the selectivity noticeably from the values obtained without hydrogen. For 5Pt−5V, there was a 4% decrease in the selectivity with increasing conversion over the tested range when hydrogen was cofed.

To count the fraction of surface Pt in the alloy and properly normalize the propylene production rate, XAS data were collected for each sample in the reduced state and after exposing the sample to air at room temperature. The basis of measuring dispersion by this method comes from the fractional Pt−O coordination arising from surface oxidized Pt. In an oxidized particle with 100% dispersion, each Pt(II) ion will have four oxygen neighbors (platinum oxide). As the dispersion decreases from unity, the Pt−O coordination number represents the fraction of the sample that is oxidized and is proportional to the dispersion. The same methodology of surface oxidation is the basis of H_2−O_2 titration, but because of the element specificity of EXAFS, the confounding effect of V oxidation on the titration is avoided, and additional structural information about the surface can be obtained.

Figure 6 shows the EXAFS difference spectra for 2Pt−5V and 5Pt−5V; fitting parameters for the difference spectra are given in Table 2. Three peaks are present in the difference spectra. The first peak at low R (at about 1.5 Å phase uncorrected distance) is characteristic of Pt−O scattering. For the 2Pt−5V sample, fitting the peak gave a bond distance of 2.05 Å and a gain in average Pt−O coordination number of

https://dx.doi.org/10.1021/acsaem.9b01373
ACS Appl. Energy Mater. 2020, 3, 1410−1422

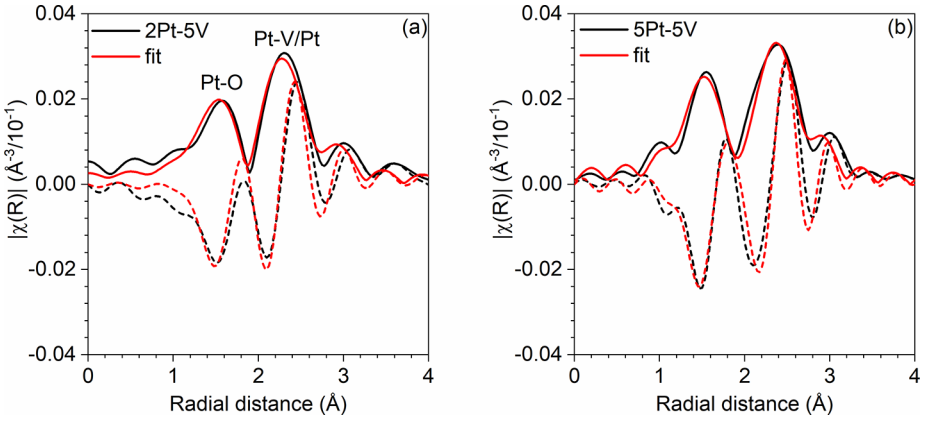

Figure 6. Pt L_3 edge EXAFS difference spectra for 2Pt−5V (a) and 5Pt−5V (b) (magnitude: solid black; imaginary: dashed black) and difference spectra fit (magnitude fit: solid red; imaginary fit: dashed red). A reduced scan of both 2Pt−5V and 5Pt−5V was taken at room temperature in He after reduction at 550 °C in 3.5% H_2; subsequently, the samples were exposed to air for 30 min and then scanned again.

Table 2. EXAFS Fit for Pt−V Difference Spectra

sample	path	CN	R (Å)	σ^2 (Å^2)	E_0 (eV)
5P−5V	Pt−O	0.6	2.03	0.002	−4.5
	Pt−Pt	1.2	2.74	0.002	−3.0
	Pt−V	0.7	2.74	0.002	4.4
2Pt−5V	Pt−O	0.5	2.05	0.002	−4.4
	Pt−Pt	0.9	2.70	0.003	2.1
	Pt−V	0.6	2.72	0.003	−3.2

0.5, which corresponds to a dispersion of 0.13. The two peaks between 2 and 3.5 Å (phase uncorrected distance) are due to lost Pt−Pt and Pt−V scattering. Fitting these peaks in the 2Pt−5V sample gives a Pt−Pt bond distance of 2.72 Å with a coordination number of 0.9 and a Pt−V bond distance of 2.70 Å with a coordination number of 0.6. Within the error of the small features in the difference spectrum, the surface layer Pt−V:Pt−Pt neighbor ratio for 2Pt−5V matches the total sample neighbor ratio.

The 5Pt−5V sample has a Pt−O coordination number of 0.6 at 2.03 Å, corresponding to a dispersion of 0.15. The bond distance for Pt−Pt and Pt−V was 2.74 Å with 1.2 and 0.7 Pt−Pt and Pt−V average coordination numbers, respectively, giving a Pt−V:Pt−Pt neighbor ratio close to 0.5. The surface ratio of 0.5 is significantly higher than the total sample neighbor ratio of 0.31, showing that the surface composition in the 5Pt−5V sample is different than that of the total sample. For both catalysts, the EXAFS difference analysis is consistent with a Pt_3V surface structure.

With the Pt dispersion from difference XAS, the initial propylene production turnover rates were calculated from catalyst test data. Note that dispersion values measured by CO chemisorption for both alloy samples were also below 20%, demonstrating the ability of the difference XAS technique to accurately determine dispersion; however, because of the possibility of metallic V adsorbing CO, dispersion values from difference XAS were used for rate normalization. The values obtained by difference XAS should be considered a lower bound on dispersion due to the possibility of surface vanadium oxide blocking chemisorption sites. Turnover rate measurements were conducted at 550 °C with differential propane conversion (<10%) and a propane concentration of 2.5%,. When hydrogen was cofed, the concentration was 2.5%. The pure Pt catalyst had a dispersion of 29% and a turnover rate of 0.36 s^{-1} when hydrogen was cofed and 0.03 s^{-1} without hydrogen. The 5Pt−5V catalyst had a dispersion of 15% and a turnover rate of 0.28 s^{-1}, while the 2Pt−5V catalyst had a dispersion of 13% and a higher turnover rate of 0.38 s^{-1}. When tested without hydrogen, 5Pt−5V had an initial TOR of 0.06 s^{-1} and 2Pt−5V had an initial TOR of 0.16 s^{-1}. The small differences between the samples under equivalent conditions are within the error generally assumed for the reproducibility of determining turnover rates.[42]

DFT. To better understand the electronic effect of V incorporation in Pt when forming Pt_3V alloys, DFT calculations were conducted on model Pt_3V (111) and Pt (111) surfaces. First, compositional phase stability of various Pt−V alloys was studied by constructing a 0 K isothermal−isobaric binary compositional phase diagram, shown in Figure 7. Finite temperature effects are not expected to significantly

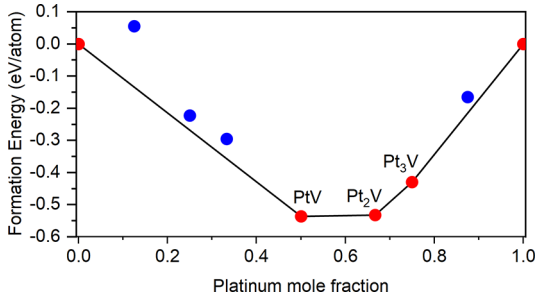

Figure 7. Binary compositional phase diagram for Pt−V. Red nodes are stable phases lying on the convex hull (black line). Blue nodes are the most stable phases for given Pt−V compositions which do not lie on the convex hull.

impact the formation energy of the concerned alloys and hence are not considered. Each point on the plot is the most thermodynamically stable bulk structure, considering fcc, hcp, and bcc crystal structures in each case, for the given composition of Pt−V. The most stable phases are connected through a convex hull and represented by red points. Unstable phases lie above the convex hull (plotted in blue) and would decompose into nearest stable phase on the convex hull, with compositions predicted by the lever rule. Apart from pure bulk Pt, the Pt_3V phase is the only stable close-packed fcc phase. This result is fully consistent with the experimental XRD and XAS measurements, which also point to the presence of a Pt_3V alloy phase with an fcc crystal structure.

https://dx.doi.org/10.1021/acsaem.9b01373
ACS Appl. Energy Mater. 2020, 3, 1410−1422

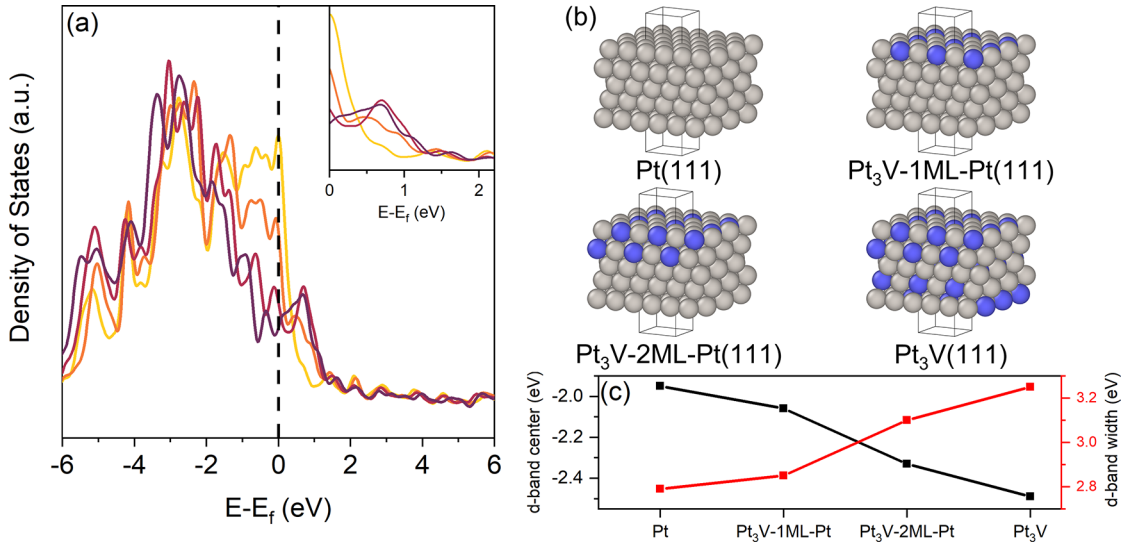

Figure 8. (a) pDOS for Pt (gold), Pt_3V (burgundy), and two epitaxial structures with one (orange) and two (crimson) layers of Pt_3V on Pt with the Fermi energy marked by a vertical dashed line. The inset graph shows an expanded view of near-Fermi energy unfilled states. (b) Structures corresponding to each model. (c) The d-band center and d-band width for the above structures.

The effect of V incorporation on the Pt electronic energy levels was studied by examining the calculated atom projected density of states of the Pt 5d band (Figure 8). Four geometries were modeled to represent pure Pt, a core−shell structure with two different shell thicknesses, and pure Pt_3V. For modeling of the core−shell structures, the topmost and top two layers of a Pt slab were replaced with Pt_3V, labeled as Pt_3V-1 ML-Pt and Pt_3V-2 ML-Pt, respectively. Starting from Pt, replacing subsequent layers of the slab with Pt_3V causes a decrease in the density of states at the Fermi level and the creation of new unoccupied states farther from the Fermi level. Pt occupied states broaden and shift to occupy lower energies with increasing V incorporation, with the most significant changes in density concentrated slightly below the Fermi energy. This shift results in the Pt d-band center decreasing from −1.95 eV for pure Pt to −2.49 eV for bulk Pt_3V. The binding strength of CO and C_1 adsorbates (Table S5) on the four slabs decreased as the alloy layer was thickened, in line with shifts in the d-band center. The degree of band filling is nearly constant for all Pt atoms in the surface and bulk alloys studied, suggesting that charge transfer to or from the d-band in the system is minimal, in agreement with previous calculations on Pt bimetallics.[5,16]

The consequences of d-band modification from V incorporation can be seen in the weakening of binding energy of adsorbates important to the dehydrogenation reaction network. The binding energies for hydrocarbon adsorbates (C_1−C_3) and hydrogen are shown in Tables S6 and S7, respectively. All hydrocarbons bind more weakly on Pt_3V as compared to Pt, and hydrogen no longer binds isoenergetically on all Pt sites in the alloy. The strongest decreases are seen in adsorbates that involve bonding to multiple surface atoms, such as is the case with deeply dehydrogenated species such as C_3H_5 and ethylidyne. The strain contribution to the binding energy changes (Table S8), calculated by fixing the lattice parameter of a Pt slab to that of Pt_3V and repeating adsorption calculations, was found to be within DFT error. Adsorbates that bond at hollow sites also bond at V containing ensembles, despite the presence of structurally equivalent Pt-only hollow sites (Figure S8).

Additionally, an often-used selectivity descriptor for dehydrogenation, the energy difference between propylene desorption and propylene dehydrogenation (Figure S9), predicts that desorption of propylene is more energetically favorable than deep dehydrogenation on Pt_3V. The change in energetics is mainly due to the destabilization of propylene, as the barrier for propylene dehydrogenation between Pt and Pt_3V differs by only 0.1 eV. The propylene dehydrogenation transition state and C_3H_5 are also both destabilized relative to gas phase propylene.

DISCUSSION

Structural Model. There are several possibilities for the arrangement of Pt and V in a bimetallic nanoparticle. The bulk Pt−V phase diagram lists five stable phases: Pt_8V, Pt_3V, Pt_2V, PtV, and PtV_3. Pt can form a solid solution with V, but the solubility (which decreases with temperature) is limited to 15 at. % V at 400 °C.[43] From the isothermal−isobaric phase diagram, Pt_3V, Pt_2V, and PtV were identified as thermodynamically stable phases.

The primary reflections in XRD of the 5Pt−5V sample rule out the non-fcc Pt−V phases which include Pt_8V, Pt_2V, and PtV. The $AuCu_3$ form of PtV_3 can be ruled out based on the presence of Pt−Pt nearest neighbors seen in EXAFS, which are not present in PtV_3. In samples that are Pt-rich with respect to Pt_3V, a phase mixture of Pt and Pt_3V form, rather than a solid solution based on asymmetric peak shapes seen in XRD. Rather than separate particles of Pt and Pt_3V, the phase mixture takes the form of a core−shell structure with a Pt_3V shell and a Pt core based on the surface composition matching Pt_3V while the total composition was Pt-rich with respect to Pt_3V.

The atomic environment of Pt in Pt_3V is cuboctohedral with eight Pt neighbors and four V neighbors, both at a bond distance of 2.74 Å. As the particle size decreases, the total coordination number and bond distance both decrease, but the ratio of V to Pt neighbors will remain constant between nanophase and bulk Pt_3V because of the local Pt environment inherent to the phase. Thus, the Pt−Pt and Pt−V coordination

https://dx.doi.org/10.1021/acsaem.9b01373
ACS Appl. Energy Mater. 2020, 3, 1410−1422

numbers can be used to determine whether a sample has a stoichiometry consistent with the Pt_3V phase.

For the 5Pt−5V, the Pt−V:Pt−Pt neighbor ratio is lower than bulk Pt_3V, indicating that the sample is Pt-rich with respect to Pt_3V. Surface oxidation difference XAS and XRD demonstrated that the phase arrangement is a core−shell particle with a Pt core and a Pt_3V shell. Because Pt−V scattering arises from the formation of Pt_3V, the Pt−Pt coordination number can be separated into Pt−Pt coordination in the alloy and Pt−Pt coordination in the Pt core, as the ratio of Pt−V to Pt−Pt in the alloy is fixed at 0.5. This allows for the fraction of each phase to be derived from the total coordination number. For 5Pt−5V, the Pt−V coordination number of 2.0 gives a total Pt_3V coordination of 6 (2 Pt−V + 4 Pt−Pt); the total coordination of 8.5 gives an alloy phase fraction of 70% and a Pt core phase fraction of 30%. Given the volume average particle size (2.2 nm) and measured lattice parameter (3.88 Å), the alloy shell layer thickness can be estimated as in ref 44, giving a shell layer thickness of 4 Å on a core 14 Å in diameter. A 4 Å shell layer corresponds to approximately 2−3 atomic layers of alloy.

In the 2Pt−5V, the Pt−V:Pt−Pt neighbor ratio matches bulk Pt_3V. Based on the XRD results for 5Pt−5V, the interpretation most consistent with the EXAFS would be that the 2Pt−5V sample is pure phase Pt_3V. The surface oxidation difference EXAFS data show that the surface stoichiometry also matches that of Pt_3V and demonstrates that no surface segregation occurs under reducing conditions. Additionally, the surface EXAFS suggests that there are few, if any, unalloyed Pt nanoparticles in this sample.

The importance of phase purity in the measurement of electronic modifications is shown in Figure 9, which shows the

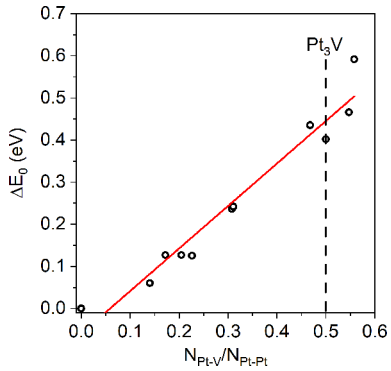

Figure 9. Pt L_3 edge XANES shift (vs Pt foil) plotted against the ratio of Pt−V to Pt−Pt coordination numbers for 3Pt and 10 Pt−V catalysts. The Pt−V to Pt−Pt ratio for the bulk Pt_3V phase is shown as a vertical dashed line. A linear fit of the data is shown in red.

Pt L_3 XANES edge energy shift relative to Pt foil as a function of the V:Pt neighbor ratio for 11 Pt−V catalysts of different composition. The neighbor ratio expected for Pt_3V is 0.5; values below this are phase mixtures of Pt and Pt_3V which have XANES edge energies lower than that of pure phase Pt_3V. In the pure phase, the XANES shift is 0.4 eV, which reflects an increase in the energy of the Pt 5d unfilled states in the alloy. Samples that are not phase pure then underestimate the electronic modification inherent to Pt_3V. Further electronic characterization was done only on the pure phase Pt_3V sample, 2Pt−5V, which allowed for more accurate comparison with the Pt_3V slab models. While this choice of a slab model neglects the contribution of corner and edge atoms in the electronic structure calculations, the experimental techniques used to characterize the catalysts are bulk sensitive and probe all Pt atoms. The majority of atoms in a 2 nm nanoparticle are terrace or interior atoms, and their electronic structure is properly captured in the slab model. While adsorption energies on terrace sites may vary significantly from corner and edge sites, scaling relationships on metals have been reported as a function of the adsorption sites' metal coordination number, and hence the trend in binding energy between Pt and Pt_3V can be captured without explicitly considering all sites.[45]

Nature of Electronic Modification. Frequently in the metal catalysis literature, the rigid band model is invoked to describe the mechanism of electronic modification of catalysts.[11−13,46,47] This model has been successfully used to describe thermal and electronic properties of alloys, which are properties dominated by conduction band s- and p-electrons, whereas in metal catalysis the localized d-electrons are responsible for catalytic behavior.[48] In the rigid band model, when two elements of different electronegativity are combined in an alloy, the atom with lower electronegativity transfers electron density to the other.[49,50] This is interpreted to further fill the d-band, shifting the Fermi energy relative to the band while the shape and absolute energy of the band remain constant. The model of charge transfer has been extended to describe not only electronic changes in alloys[11,12,51] but also nanoparticle−support interactions[52] and particle size effects.[53] These observations of electronic modification are based on spectral changes seen in various techniques sensitive to valence d-electrons such as XPS, XANES, and ELNES, among others. Using this model, one could predict the direction and magnitude of electron transfer for a given alloy and hence the spectral changes in XPS, XANES, and RIXS. If electron transfer to the d-band accurately describes the mechanism of electronic modification of Pt, the direction of charge transfer predicted should be consistent among these methods.

The Pt L_3 edge XANES transition probability is proportional to the number of unfilled states, and changes in the intensity and broadness of the XANES white line reflect changes in the density of Pt 5d unfilled states.[54,55] The rigid band model has also been used to describe these spectral changes in the XANES.[11,50] In this interpretation, the transfer of electron density to Pt decreases the number of unfilled Pt 5d states (i.e., more d-electron density), leading to a lower white line intensity. Additionally, because of the increased filling of the d-band resulting from the electron transfer, the average energy of the unfilled states increases which causes an increase in the XANES edge energy. By the above model, the 0.4 eV increase in XANES edge energy seen for Pt_3V would mean that Pt in Pt_3V has gained electrons through electron transfer from V. The increase in the number of Pt electrons would also be expected to lead to a decrease in the white line intensity; however, the white line intensity increases relative to a Pt nanoparticle of the same size.

XPS binding energy shifts are also frequently used demonstrate electronic modification resulting from alloying. Chemical shifts in XPS are frequently interpreted based on electron transfer, as the energy required for photoemission is greater in a positively charged atom and vice versa for a negatively charged atom. Based on this interpretation, the 0.4 eV core level shift to higher binding energy seen for Pt_3V is due to Pt in the alloy having transferred electrons to V. It should be noted that the orbital to which the electron is

https://dx.doi.org/10.1021/acsaem.9b01373
ACS Appl. Energy Mater. 2020, 3, 1410−1422

transferred is not specified, but unfilled states exist in the 5d or conduction band 6s or 6p orbitals. By use of the same electron transfer model, XANES and XPS come to opposite conclusions regarding the direction of the transfer.

While XANES and XPS allow for an indirect measurement of filled d-states, RIXS is a direct measurement. The inelastic scattering peak in RIXS represents the energy difference between the weighted average energy of the filled and unfilled states. By the rigid band model, any change in filling of the d-band would shift the average energy of the filled and unfilled states in the same direction. Hence, the separation in energy between the filled and unfilled states should be similar regardless of any electron transfer. Based on the separately collected XANES spectrum, the energy transfer value can be deconvoluted into a downward shift in the filled state energy and an upward shift in energy of the unfilled state energy, which cannot be explained by electron transfer.

The inconsistency between the predicted direction of electron transfer in XPS, XANES, and the increased separation energy between the filled and unfilled states by RIXS suggests that the rigid band model and electron transfer between the Pt d-band and the promoter atom is incorrect. For Pt and Pt_3V, the density of states calculations demonstrate that the alloy does not follow rigid band behavior. Instead, the d-band of Pt_3V is broadened with respect to Pt, resulting in changes the energy of the filled and unfilled 5d states. These energy changes are consistent with the spectral changes observed by XPS, XANES, and RIXS. For example, the broadening of the d-band causes the d-band center to shift away from the Fermi level, decreasing the average energy of the filled states, consistent with the RIXS results. The unfilled Pt 5d states also increase in energy due to the broadening of the band, resulting in an increase in the XANES edge energy in Pt_3V. Despite this modification in the density of states, the filling of the d-band (and hence number of d-electrons) remains constant, as shown by the integration of the d-band density of states for Pt and Pt_3V. The increased splitting in the energy of the filled and unfilled d-states is a consequence of bonding interactions between Pt and V which form new d-states that differ in energy from those in a homoatomic bond. Thus, it is a change in the energy of the filled and unfilled d-states that gives rise to the changes in the XPS, XANES, and RIXS spectra of Pt_3V. While the above results do not preclude electron transfer to Pt s- and p-bands, these electrons are minimally involved in adsorbate binding, and hence transfer to these orbitals would be largely inconsequential as far as catalytic properties are concerned. Inferring changes to the d-band from XPS alone should be made with caution since core level shifts in alloys are sensitive to changes in energy, number, and orbital character of the valence electrons as well as extra-atomic relaxations and shifts in the Fermi energy.[56,57] See Figure S10 and Table S9 as well as the supplemental discussion for a more comprehensive examination of the contribution of various effects to the XPS core level shifts and their interpretation.

The consequence of these electronic effects can be seen in decrease in binding strength of adsorbates on the Pt_3V alloy vs monometallic Pt surfaces (Table S6). All the model adsorbates considered, including CH_x, CCH_3, C_3H_6, and C_3H_5, showed weakening in binding energy compared to their binding strength on pure Pt. Because alloying decreases the average energy of the filled 5d states, the binding strength of adsorbates weakens as predicted by d-band theory.[6] It has been proposed that this weakening of adsorption strength leads to the desorption pathway being favored over deep dehydrogenation in DFT studies of Pt−Sn alloys.[58] As seen from Figure S9, a similar conclusion can be drawn for Pt_3V since the thermodynamics of deep dehydrogenation compared to desorption are competitive in the case of Pt_3V, while for monometallic Pt the deep dehydrogenation is clearly thermodynamically favored.

Effect of Structure on Catalytic Performance. The structural characterization explains why 5Pt−5V and 2Pt−5V have close to identical propylene selectivities and dehydrogenation turnover rates despite the particle composition being different in each catalyst. The reason is that the surface and near-surface layers which affect catalytic properties are compositionally the same. The geometric effect only requires the presence of V atoms in the surface layer, whereas the electronic effect is affected by both the surface and subsurface. The surface alloy layer in 5Pt−5V is 2−3 atomic layers thick, meaning that the nearest neighbors of surface atoms participating in catalysis, both surface and subsurface, are the same as in the pure alloy catalyst. The importance of the subsurface layer on catalytic properties was demonstrated in the difference in CO heat of adsorption between a Pt_3Mn full alloy and a Pt/Pt_3Mn core−shell catalyst.[59] The electronic effect occurs as a result of bonds between the active metal and the promoter. Because of this nature, electronic modification is necessarily a short-range effect, as demonstrated by surface Pt density of states, which showed a large change when first nearest neighbors were changed, as compared to the small change which occurred between the two monolayer slab and the full alloy where only second nearest neighbors of the surface Pt atoms are changed.

The geometric effect, or the decreasing the active metal ensemble size, requires the presence of the promoter metal in the surface layer of the nanoparticle. Difference XAS spectra on Pt−V alloys demonstrate that V is present in the surface layer. The geometric effect is often cited as the dominant factor in dehydrogenation selectivity in alloys where the active metal is isolated.[18,60,61] However, in the case of Pt_3V, the (111) surface is composed of interconnected groups of three Pt atoms. Despite the lack of total Pt isolation, Pt_3V still shows above 95% propylene selectivity, which suggests that total Pt isolation is not a requirement for high dehydrogenation selectivity. This conclusion is supported by DFT results, which show that Pt_3V alloys bind C_2 and C_3 intermediates more weakly on sites of different geometry as compared to pure Pt, in spite of the presence of threefold Pt sites geometrically equivalent to Pt on the Pt_3V surface.

It is also worth mentioning that mechanisms proposed for the hydrogenolysis of alkanes vary in the number of metal sites required for the reaction from two to more than four.[62−65] DFT studies on various metals have shown that the barrier for C−C bond cleavage lowers as more hydrogen atoms are removed from the adsorbed hydrocarbon.[66] Based on these results, the mechanism for hydrogenolysis is suggested to occur through a deeply dehydrogenated species. For every hydrogen lost to dehydrogenation, the C−H bond is replaced with a metal−carbon bond.[67] Thus, the extent of dehydrogenation at which hydrogenolysis occurs determines the number of active metal atoms needed to catalyze the reaction. Even assuming the high-end ensemble size requirements for hydrogenolysis (4+ atoms), the (111) surface of Pt_3V should still have a large enough active metal ensemble to catalyze hydrogenolysis. A possible reason that these sites, which are important for

https://dx.doi.org/10.1021/acsaem.9b01373
ACS Appl. Energy Mater. 2020, 3, 1410−1422

stabilization of coke precursors on Pt,[68] do not cause low selectivity in Pt_3V may be due to the decreased binding strength and change of binding geometry of coke precursors shown in Figure S8 and Table S6. The surface and subsurface V atoms proximal to the 3-fold site electronically modify Pt destabilizing adsorption on this site.

CONCLUSIONS

The addition of V to a Pt catalyst leads to the formation of the Pt_3V intermetallic compound with the $AuCu_3$ structure. The formation of the Pt_3V phase, or an alloy surface layer on a Pt core, led to high propylene selectivity, demonstrating that total Pt site isolation, and full alloy formation, are not required for high dehydrogenation selectivity. Instead, it is only necessary to form an alloy layer 2−3 atomic layers thick to obtain the same performance as a pure phase alloy. Formation of the ordered alloy phase ensures that all Pt atoms in the nanoparticle experience similar electronic modification and that large Pt ensembles are eliminated. Other unexplored alloys with the $AuCu_3$ structure may also show high dehydrogenation selectivity based on the high selectivity of both Pt_3Sn and Pt_3V despite very different bonding interactions between Pt and the promoting element. The magnitude of the electronic modification was shown to be dependent on the extent of alloy formation, demonstrating the importance of phase purity in determining the electronic modification inherent to a specific alloy phase. The source of electronic modification in Pt−V alloys is not caused by electron transfer to or from the Pt 5d orbitals, but rather a change in the energy of the orbitals. The consequences of the electronic modification were shown by DFT to be weakening of adsorbate bonding to Pt and changes in the most stable binding geometries in the alloy.

ASSOCIATED CONTENT

Supporting Information

The Supporting Information is available free of charge at https://pubs.acs.org/doi/10.1021/acsaem.9b01373.

Figures S1−S10 and Tables S1−S9 (PDF)

AUTHOR INFORMATION

Corresponding Author

Jeffrey T. Miller − *Davidson School of Chemical Engineering, Purdue University, West Lafayette, Indiana 47907, United States;* orcid.org/0000-0002-6269-0620; Email: mill1194@purdue.edu

Other Authors

Stephen C. Purdy − *Davidson School of Chemical Engineering, Purdue University, West Lafayette, Indiana 47907, United States*

Pushkar Ghanekar − *Davidson School of Chemical Engineering, Purdue University, West Lafayette, Indiana 47907, United States*

Garrett Mitchell − *Davidson School of Chemical Engineering, Purdue University, West Lafayette, Indiana 47907, United States*

A. Jeremy Kropf − *Chemical Sciences and Engineering Division, Argonne National Laboratory, Argonne, Illinois 60439, United States*

Dmitry Y. Zemlyanov − *Birck Nanotechnology Center, Purdue University, West Lafayette, Indiana 47907, United States*

Yang Ren − *X-ray Sciences Division, Argonne National Laboratory, Argonne, Illinois 60439, United States;* orcid.org/0000-0001-9831-6035

Fabio Ribeiro − *Davidson School of Chemical Engineering, Purdue University, West Lafayette, Indiana 47907, United States*

W. Nicholas Delgass − *Davidson School of Chemical Engineering, Purdue University, West Lafayette, Indiana 47907, United States*

Jeffrey Greeley − *Davidson School of Chemical Engineering, Purdue University, West Lafayette, Indiana 47907, United States;* orcid.org/0000-0001-8469-1715

Complete contact information is available at: https://pubs.acs.org/10.1021/acsaem.9b01373

Author Contributions

S.C.P. and P.G. contributed equally to this work.

Notes

The authors declare no competing financial interest.

ACKNOWLEDGMENTS

This paper is based upon work supported in part by the National Science Foundation under Cooperative Agreement EEC-1647722. Use of the advanced photon source was supported by the U.S. Department of Energy, Office of Basic Energy Sciences, under Contract DE-AC02-06CH11357. MRCAT operations, beamline 10-BM and 10-ID, are supported by the Department of Energy and the MRCAT member institutions. The authors also acknowledge the use of the 11-ID-C beamline at the advanced photon source. XPS data were collected at the Surface Analysis Facility of the Birck Nanotechnology Center of Purdue University. Use of the Center for Nanoscale Materials (CNM), a U.S. Department of Energy, Office of Science, Office of Basic Energy Sciences User Facility, Information Technology at Purdue (West Lafayette, IN), and computational resources from the National Energy Research Scientific Computing Center is gratefully acknowledged. This material is based upon work supported, in part, by the U.S. Department of Energy Office of Science, Office of Basic Energy Sciences, Chemical Sciences, Geosciences, & Biosciences (CSBG) division. The authors acknowledge Joseph Kubal, Brandon Bukowski, and Siddharth Deshpande for valuable discussions.

REFERENCES

(1) Furukawa, S.; Komatsu, T. Intermetallic Compounds: Promising Inorganic Materials for Well-Structured and Electronically Modified Reaction Environments for Efficient Catalysis. *ACS Catal.* **2017**, *7* (1), 735−765.

(2) Sinfelt, J. H.; Yates, D. J. C. Catalytic Hydrogenolysis of Ethane over the Noble Metals of Group VIII. *J. Catal.* **1967**, *8* (1), 82−90.

(3) Bhasin, M.; McCain, J.; Vora, B.; Imai, T.; Pujadó, P. Dehydrogenation and Oxydehydrogenation of Paraffins to Olefins. *Appl. Catal., A* **2001**, *221* (1−2), 397−419.

(4) Sattler, J. J. H. B.; Ruiz-Martinez, J.; Santillan-Jimenez, E.; Weckhuysen, B. M. Catalytic Dehydrogenation of Light Alkanes on Metals and Metal Oxides. *Chem. Rev.* **2014**, *114* (20), 10613−10653.

(5) Kitchin, J. R.; Nørskov, J. K.; Barteau, M. A.; Chen, J. G. Modification of the Surface Electronic and Chemical Properties of Pt(111) by Subsurface 3d Transition Metals. *J. Chem. Phys.* **2004**, *120* (21), 10240−10246.

(6) Hammer, B.; Nørskov, J. K. Electronic Factors Determining the Reactivity of Metal Surfaces. *Surf. Sci.* **1995**, *343* (3), 211−220.

(7) Natal-Santiago, M. A.; Podkolzin, S. G.; Cortright, R. D.; Dumesic, J. A. Microcalorimetric Studies of Interactions of Ethene, Isobutene, and Isobutane with Silica-Supported Pd, Pt, and PtSn. *Catal. Lett.* **1997**, *45* (3-4), 155−163.
(8) Cortright, R. D.; Dumesic, J. A. Microcalorimetric, Spectroscopic, and Kinetic Studies of Silica Supported Pt and Pt/Sn Catalysts for Isobutane Dehydrogenation. *J. Catal.* **1994**, *148* (2), 771−778.
(9) Nykänen, L.; Honkala, K. Density Functional Theory Study on Propane and Propene Adsorption on Pt(111) and PtSn Alloy Surfaces. *J. Phys. Chem. C* **2011**, *115* (19), 9578−9586.
(10) Nykänen, L.; Honkala, K. Selectivity in Propene Dehydrogenation on Pt and Pt 3 Sn Surfaces from First Principles. *ACS Catal.* **2013**, *3* (12), 3026−3030.
(11) Sun, P.; Siddiqi, G.; Vining, W. C.; Chi, M.; Bell, A. T. Novel Pt/Mg(In)(Al)O Catalysts for Ethane and Propane Dehydrogenation. *J. Catal.* **2011**, *282* (1), 165−174.
(12) Siri, G. J.; Ramallo-López, J. M.; Casella, M. L.; Fierro, J. L. G.; Requejo, F. G.; Ferretti, O. A. XPS and EXAFS Study of Supported PtSn Catalysts Obtained by Surface Organometallic Chemistry on Metals. *Appl. Catal., A* **2005**, *278* (2), 239−249.
(13) Greiner, M. T.; Jones, T. E.; Beeg, S.; Zwiener, L.; Scherzer, M.; Girgsdies, F.; Piccinin, S.; Armbrüster, M.; Knop-Gericke, A.; Schlögl, R. Free-Atom-like d States in Single-Atom Alloy Catalysts. *Nat. Chem.* **2018**, *10* (10), 1008.
(14) Chen, W.; Schneider, W. F.; Wolverton, C. Trends in Atomic Adsorption on Pt 3 M(111) Transition Metal Bimetallic Surface Overlayers. *J. Phys. Chem. C* **2014**, *118* (16), 8342−8349.
(15) Friedrich, M.; Ormeci, A.; Grin, Y.; Armbrüster, M. PdZn or ZnPd: Charge Transfer and Pd-Pd Bonding as the Driving Force for the Tetragonal Distortion of the Cubic Crystal Structure. *Z. Anorg. Allg. Chem.* **2010**, *636* (9−10), 1735−1739.
(16) Schweitzer, N.; Xin, H.; Nikolla, E.; Miller, J. T.; Linic, S. Establishing Relationships Between the Geometric Structure and Chemical Reactivity of Alloy Catalysts Based on Their Measured Electronic Structure. *Top. Catal.* **2010**, *53* (5−6), 348−356.
(17) Nikolla, E.; Schwank, J.; Linic, S. Measuring and Relating the Electronic Structures of Nonmodel Supported Catalytic Materials to Their Performance. *J. Am. Chem. Soc.* **2009**, *131* (7), 2747−2754.
(18) Cybulskis, V. J.; Bukowski, B. C.; Tseng, H. T.; Gallagher, J. R.; Wu, Z.; Wegener, E.; Kropf, A. J.; Ravel, B.; Ribeiro, F. H.; Greeley, J.; Miller, J. T. Zinc Promotion of Platinum for Catalytic Light Alkane Dehydrogenation: Insights into Geometric and Electronic Effects. *ACS Catal.* **2017**, *7* (6), 4173−4181.
(19) Mun, B. S.; Watanabe, M.; Rossi, M.; Stamenkovic, V.; Markovic, N. M.; Ross, P. N. A Study of Electronic Structures of Pt3M (M = Ti,V,Cr,Fe,Co,Ni) Polycrystalline Alloys with Valence-Band Photoemission Spectroscopy. *J. Chem. Phys.* **2005**, *123* (20), 204717.
(20) Cui, Z.; Chen, H.; Zhao, M.; Marshall, D.; Yu, Y.; Abruña, H.; DiSalvo, F. J. Synthesis of Structurally Ordered Pt 3 Ti and Pt 3 V Nanoparticles as Methanol Oxidation Catalysts. *J. Am. Chem. Soc.* **2014**, *136* (29), 10206−10209.
(21) Benson, J.; Boudart, M. Hydrogen-Oxygen Titration Method for the Measurement Areas of Supported. *J. Catal.* **1965**, *4*, 704−710.
(22) Bolin, T. B.; Wu, T.; Schweitzer, N.; Lobo-Lapidus, R.; Kropf, A. J.; Wang, H.; Hu, Y.; Miller, J. T.; Heald, S. M. In Situ Intermediate-Energy X-Ray Catalysis Research at the Advanced Photon Source Beamline 9-BM. *Catal. Today* **2013**, *205*, 141−147.
(23) Hammersley, A. P. *FIT2D: An Introduction and Overview*, 1997.
(24) Hammersley, A. P.; Svensson, S. O.; Hanfland, M.; Fitch, A. N.; Hausermann, D. Two-Dimensional Detector Software: From Real Detector to Idealised Image or Two-Theta Scan. *High Pressure Res.* **1996**, *14* (4−6), 235−248.
(25) Lutterotti, L. Total Pattern Fitting for the Combined Size-Strain-Stress-Texture Determination in Thin Film Diffraction. *Nucl. Instrum. Methods Phys. Res., Sect. B* **2010**, *268* (3−4), 334−340.
(26) Kresse, G.; Furthmüller, J. Efficiency of Ab-Initio Total Energy Calculations for Metals and Semiconductors Using a Plane-Wave Basis Set. *Comput. Mater. Sci.* **1996**, *6* (1), 15−50.
(27) Kresse, G.; Furthmüller, J. Efficient Iterative Schemes for Ab Initio Total-Energy Calculations Using a Plane-Wave Basis Set. *Phys. Rev. B: Condens. Matter Mater. Phys.* **1996**, *54* (16), 11169−11186.
(28) Kresse, G.; Hafner, J. Ab Initio Molecular Dynamics for Liquid Metals. *Phys. Rev. B: Condens. Matter Mater. Phys.* **1993**, *47* (1), 558−561.
(29) Kresse, G.; Hafner, J. Ab Initio Molecular-Dynamics Simulation of the Liquid-Metal−Amorphous-Semiconductor Transition in Germanium. *Phys. Rev. B: Condens. Matter Mater. Phys.* **1994**, *49* (20), 14251−14269.
(30) Blöchl, P. E. Projector Augmented-Wave Method. *Phys. Rev. B: Condens. Matter Mater. Phys.* **1994**, *50* (24), 17953−17979.
(31) Perdew, J. P.; Burke, K.; Ernzerhof, M. Generalized Gradient Approximation Made Simple. *Phys. Rev. Lett.* **1996**, *77* (18), 3865−3868.
(32) Monkhorst, H. J.; Pack, J. D. Special Points for Brillouin-Zone Integrations. *Phys. Rev. B* **1976**, *13* (12), 5188−5192.
(33) Methfessel, M.; Paxton, A. T. High-Precision Sampling for Brillouin-Zone Integration in Metals. *Phys. Rev. B: Condens. Matter Mater. Phys.* **1989**, *40* (6), 3616−3621.
(34) Henkelman, G.; Uberuaga, B. P.; Jónsson, H. A Climbing Image Nudged Elastic Band Method for Finding Saddle Points and Minimum Energy Paths. *J. Chem. Phys.* **2000**, *113* (22), 9901−9904.
(35) Hjorth Larsen, A.; Jørgen Mortensen, J.; Blomqvist, J.; Castelli, I. E; Christensen, R.; Dułak, M.; Friis, J.; Groves, M. N; Hammer, B.; Hargus, C.; Hermes, E. D; Jennings, P. C; Bjerre Jensen, P.; Kermode, J.; Kitchin, J. R; Leonhard Kolsbjerg, E.; Kubal, J.; Kaasbjerg, K.; Lysgaard, S.; Bergmann Maronsson, J.; Maxson, T.; Olsen, T.; Pastewka, L.; Peterson, A.; Rostgaard, C.; Schiøtz, J.; Schutt, O.; Strange, M.; Thygesen, K. S; Vegge, T.; Vilhelmsen, L.; Walter, M.; Zeng, Z.; Jacobsen, K. W The Atomic Simulation Environment - A Python Library for Working with Atoms. *J. Phys.: Condens. Matter* **2017**, *29*, 273002.
(36) Stukowski, A. Visualization and Analysis of Atomistic Simulation Data with OVITO-the Open Visualization Tool. *Modell. Simul. Mater. Sci. Eng.* **2010**, *18* (1), 015012.
(37) Miller, J. T.; Kropf, A. J.; Zha, Y.; Regalbuto, J. R.; Delannoy, L.; Louis, C.; Bus, E.; van Bokhoven, J. A. The Effect of Gold Particle Size on AuAu Bond Length and Reactivity toward Oxygen in Supported Catalysts. *J. Catal.* **2006**, *240* (2), 222−234.
(38) Bus, E.; Van Bokhoven, J. A. Electronic and Geometric Structures of Supported Platinum, Gold, and Platinum-Gold Catalysts. *J. Phys. Chem. C* **2007**, *111* (27), 9761−9768.
(39) Waterstrat, R. M. The Vanadium-Platinum Constitution Diagram. *Metall. Trans. A* **1973**, *4* (2), 455−466.
(40) Leontyev, I. N.; Kuriganova, A. B.; Leontyev, N. G.; Hennet, L.; Rakhmatullin, A.; Smirnova, N. V.; Dmitriev, V. Size Dependence of the Lattice Parameters of Carbon Supported Platinum Nanoparticles: X-Ray Diffraction Analysis and Theoretical Considerations. *RSC Adv.* **2014**, *4* (68), 35959−35965.
(41) Moulder, J. F.; Stickle, W. F.; Sobol, P. E.; Bomben, K. D. *Handbook of X-Ray Photoelectron Spectroscopy*; Chastain, J., King, R. C. J., Eds.; Physical Electronics, Inc.: Eden Prairie, MN, 1995.
(42) Ribeiro, F. H.; Schach Von Wittenau, A. E.; Bartholomew, C. H.; Somorjai, G. A. Reproducibility of Turnover Rates in Heterogeneous Metal Catalysis: Compilation of Data and Guidelines for Data Analysis. *Catal. Rev.: Sci. Eng.* **1997**, *39* (1−2), 49−76.
(43) Wang, C. P.; Zheng, A. Q.; Liu, X. J. Thermodynamic Assessments of the V-Ge and V-Pt Systems. *Intermetallics* **2008**, *16* (4), 544−549.
(44) LiBretto, N. J.; Yang, C.; Ren, Y.; Zhang, G.; Miller, J. T. Identification of Surface Structures in Pt3Cr Intermetallic Nanocatalysts. *Chem. Mater.* **2019**, *31*, 1597.
(45) Calle-Vallejo, F.; Loffreda, D.; Koper, M. T. M.; Sautet, P. Introducing Structural Sensitivity into Adsorption-Energy Scaling Relations by Means of Coordination Numbers. *Nat. Chem.* **2015**, *7* (5), 403−410.
(46) Román-Martínez, M. C.; Maciá-Agulló, J. A.; Vilella, I. M. J.; Cazorla-Amorós, D.; Yamashita, H. State of Pt in Dried and Reduced

https://dx.doi.org/10.1021/acsaem.9b01373
ACS Appl. Energy Mater. 2020, 3, 1410−1422

PtIn and PtSn Catalysts Supported on Carbon. *J. Phys. Chem. C* **2007**, *111* (12), 4710−4716.
(47) Ramallo-López, J. M.; Santori, G. F.; Giovanetti, L.; Casella, M. L.; Ferretti, O. A.; Requejo, F. G. XPS and XAFS Pt L 2,3 -Edge Studies of Dispersed Metallic Pt and PtSn Clusters on SiO 2 Obtained by Organometallic Synthesis: Structural and Electronic Characteristics. *J. Phys. Chem. B* **2003**, *107* (41), 11441−11451.
(48) Nørskov, J. K. Covalent Effects in the Effective-Medium Theory of Chemical Binding: Hydrogen Heats of Solution in the 3d Metals. *Phys. Rev. B: Condens. Matter Mater. Phys.* **1982**, *26* (6), 2875−2885.
(49) Mott, N. F.; Jones, H. *The Theory of the Properties of Metals and Alloys*; Clarendon Press: Oxford, 1936.
(50) Stern, E. A. Rigid-Band Model of Alloys. *Phys. Rev.* **1967**, *157* (3), 544−551.
(51) Deng, L.; Shishido, T.; Teramura, K.; Tanaka, T. Effect of Reduction Method on the Activity of Pt-Sn/$SiO_2$for Dehydrogenation of Propane. *Catal. Today* **2014**, *232*, 33−39.
(52) Behafarid, F.; Ono, L. K.; Mostafa, S.; Croy, J. R.; Shafai, G.; Hong, S.; Rahman, T. S.; Bare, S. R.; Roldan Cuenya, B. Electronic Properties and Charge Transfer Phenomena in Pt Nanoparticles on γ-Al2O3: Size, Shape, Support, and Adsorbate Effects. *Phys. Chem. Chem. Phys.* **2012**, *14* (33), 11766.
(53) Mason, M. G. Electronic Structure of Supported Small Metal Clusters. *Phys. Rev. B: Condens. Matter Mater. Phys.* **1983**, *27* (2), 748−762.
(54) Mansour, A. N.; Cook, J. W.; Sayers, D. E. Quantitative Technique for the Determination of the Number of Unoccupied D-Electron States in a Platinum Catalyst Using the L2,3 x-Ray Absorption Edge Spectra. *J. Phys. Chem.* **1984**, *88* (11), 2330−2334.
(55) Ramaker, D. E.; Mojet, B. L.; Garriga Oostenbrink, M. T.; Miller, J. T.; Koningsberger, D. C. Contribution of Shape Resonance and Pt−H EXAFS in the Pt L2,3 X-Ray Absorption Edges of Supported Pt Particles: Application and Consequences for Catalyst Characterization. *Phys. Chem. Chem. Phys.* **1999**, *1* (9), 2293−2302.
(56) Weinert, M.; Watson, R. E. Core-Level Shifts in Bulk Alloys and Surface Adlayers. *Phys. Rev. B: Condens. Matter Mater. Phys.* **1995**, *51* (23), 17168−17180.
(57) Olovsson, W.; Göransson, C.; Pourovskii, L. V.; Johansson, B.; Abrikosov, I. A. Core-Level Shifts in Fcc Random Alloys: A First-Principles Approach. *Phys. Rev. B: Condens. Matter Mater. Phys.* **2005**, *72* (6), 1−12.
(58) Yang, M. L.; Zhu, Y. A.; Zhou, X. G.; Sui, Z. J.; Chen, D. First-Principles Calculations of Propane Dehydrogenation over PtSn Catalysts. *ACS Catal.* **2012**, *2* (6), 1247−1258.
(59) Wu, Z.; Bukowski, B. C.; Li, Z.; Milligan, C.; Zhou, L.; Ma, T.; Wu, Y.; Ren, Y.; Ribeiro, F. H.; Delgass, W. N.; Greeley, J. P.; Zhang, G.; Miller, J. T. Changes in Catalytic and Adsorptive Properties of 2 Nm Pt3Mn Nanoparticles by Subsurface Atoms. *J. Am. Chem. Soc.* **2018**, *140*, 14870.
(60) Wu, Z.; Wegener, E. C.; Tseng, H.-T.; Gallagher, J. R.; Harris, J. W.; Diaz, R. E.; Ren, Y.; Ribeiro, F. H.; Miller, J. T. Pd−In Intermetallic Alloy Nanoparticles: Highly Selective Ethane Dehydrogenation Catalysts. *Catal. Sci. Technol.* **2016**, *6* (18), 6965−6976.
(61) Childers, D. J.; Schweitzer, N. M.; Shahari, S. M. K.; Rioux, R. M.; Miller, J. T.; Meyer, R. J. Modifying Structure-Sensitive Reactions by Addition of Zn to Pd. *J. Catal.* **2014**, *318*, 75−84.
(62) Martin, G. A. The Kinetics of the Catalytic Hydrogenolysis of Ethane over Ni/SiO_2. *J. Catal.* **1979**, *60* (3), 345−355.
(63) Goddard, S. A.; Amiridis, M. D.; Rekoske, J. E.; Cardona-Martinez, N.; Dumesic, J. A. Kinetic Simulation of Heterogeneous Catalytic Processes: Ethane Hydrogenolysis over Supported Group VIII Metals. *J. Catal.* **1989**, *117* (1), 155−169.
(64) Flaherty, D. W.; Hibbitts, D. D.; Gürbüz, E. I.; Iglesia, E. Theoretical and Kinetic Assessment of the Mechanism of Ethane Hydrogenolysis on Metal Surfaces Saturated with Chemisorbed Hydrogen. *J. Catal.* **2014**, *311*, 350−356.
(65) Almithn, A.; Hibbitts, D. Effects of Catalyst Model and High Adsorbate Coverages in Ab Initio Studies of Alkane Hydrogenolysis. *ACS Catal.* **2018**, *8*, 6375−6387.
(66) Sinfelt, J. H. Specificity in Catalytic Hydrogenolysis by Metals. *Adv. Catal.* **1973**, *23*, 91−119.
(67) Watwe, R. M.; Cortright, R. D.; Nørskov, J. K.; Dumesic, J. A. Theoretical Studies of Stability and Reactivity of C_2 Hydrocarbon Species on Pt Clusters, Pt(111), and Pt(211). *J. Phys. Chem. B* **2000**, *104* (10), 2299−2310.
(68) Hook, A.; Massa, J. D.; Celik, F. E. Effect of Tin Coverage on Selectivity for Ethane Dehydrogenation over Platinum-Tin Alloys. *J. Phys. Chem. C* **2016**, *120* (48), 27307−27318.

https://dx.doi.org/10.1021/acsaem.9b01373
ACS Appl. Energy Mater. 2020, 3, 1410−1422